Helicity-dependent continuous varifocal metalens based on bilayer dielectric metasurfaces

YANQUN WANG,[1,2] LI CHEN,[3] SHIWEI TANG,[1,4,8] (iD) PEIPENG XU,[1,2,9] (iD) FEI DING,[5] (iD) ZHUORAN FANG,[6] AND ARKA MAJUMDAR[6,7] (iD)

[1]*Faculty of Electrical Engineering and Computer Science, Ningbo University, Ningbo 315211, China*
[2]*Key Laboratory of Photoelectric Detection Materials and Devices of Zhejiang Province, Ningbo 315211, China*
[3]*School of Information and Optoelectronic Science and Engineering, South China Normal University, Guangzhou 510006, China*
[4]*School of Physical Science and Technology, Ningbo University, Ningbo 315211, China*
[5]*Centre for Nano Optics, University of Southern Denmark, Campusvej 55, DK-5230 Odense, Denmark*
[6]*Department of Electrical and Computer Engineering, University of Washington, Seattle, WA 98195, USA*
[7]*Department of Physics, University of Washington, Seattle, WA 98195, USA*
[8]*tangshiwei@nbu.edu.cn*
[9]*xupeipeng@nbu.edu.cn*

Abstract: Metasurfaces offer a unique platform to realize flat lenses, reducing the size and complexity of imaging systems and thus enabling new imaging modalities. In this paper, we designed a bilayer helicity-dependent continuous varifocal dielectric metalens in the near-infrared range. The first layer consists of silicon nanopillars and functions as a half-wave plate, providing the helicity-dependent metasurface by combining propagation phase and geometric phase. The second layer consists of phase-change material Sb_2S_3 nanopillars and provides tunable propagation phases. Upon excitation with the circularly polarized waves possessing different helicities, the metalens can generate helicity-dependent longitudinal focal spots. Under the excitation of linear polarized light, the helicity-dependent dual foci are generated. The focal lengths in this metalens can be continuously tuned by the crystallization fraction of Sb_2S_3. The zoom range is achieved from 32.5 μm to 37.2 μm for right circularly polarized waves and from 50.5 μm to 60.9 μm for left circularly polarized waves. The simulated focusing efficiencies are above 75% and 87% for the circularly and linearly polarized waves, respectively. The proposed metalens has potential applications in miniaturized devices, including compact optical communication systems, imaging, and medical devices.

1. Introduction

Metasurfaces, consisting of two-dimensional subwavelength scatterers on a planar surface, can modify incident electromagnetic wave's phase, amplitude, and polarization [1–5]. In recent years, advancements in metasurfaces have driven the development of ultrathin and lightweight metadevices, including polarization converters [6–10], optical vortex generators [11–14], holograms [15,16], and metalenses [17–22]. A metalens can focus transmitted or reflected waves into diffraction-limited focal spots while maintaining a flat form factor. Unfortunately, the focal length cannot be dynamically adjusted once the metalens is fabricated. Compact varifocal lenses are important for many applications in adaptive vision [23], augmented reality [24], and imaging [25]. Current varifocal imaging systems are implemented via tuning the relative distance between bulky optical elements, which are unsuitable for miniaturized systems. Compact varifocal metalenses can potentially provide an attractive solution.

Up to now, many methods have been proposed to demonstrate varifocal metalenses such as microelectromechanical systems (MEMS) [26–28], stretching elastic substrate [29–31], controlling the relative orientation between two compound metalens [32–35], and laterally actuating two separate metalenses [36,37]. Nevertheless, these metalenses all require mechanical moving parts which cannot operate in turbulent environments such as high altitudes. MEMS-based meta-optics are also challenging to fabricate and could potentially be of low fabrication yield. Another effective strategy is to incorporate tunable or active materials into metalenses to change the focal length, such as graphene [38,39], anisotropic liquid crystals [40,41], and phase-change materials [42–44]. However, the varifocal metalens based on changing the Fermi level of graphene usually suffers from a limited zoom range, and the focusing efficiency is significantly affected by the graphene absorption. Although liquid crystals can be integrated into metalenses to tune the focal length, continuous varifocal capability or high focusing efficiency is difficult to achieve. Varifocal metalenses based on phase-change materials $Ge_2Sb_2Te_5$ (GST) or $Ge_2Sb_2Se_4Te_1$ (GSST) have also been realized; however, focusing efficiencies are intrinsically limited by the strong absorption loss of GST and GSST in visible and near IR wavelengths [42–44]. An emerging phase-change material, Sb_2S_3 has recently attracted much attention because of ultralow loss in the near-infrared and stable intermediate states [45–49]. Additionally, Sb_2S_3 exhibits a refractive index contrast of $\Delta n \approx 0.6$ at the wavelength of 1550 nm and a high transition temperature of 270 °C [46], making it thermally stable. These superior properties have already led to the application of Sb_2S_3 in dynamic filters [47,48] and non-volatile microring switches [49].

Recently, Pancharatnam-Berry (PB) phase metasurfaces have shown excellent capabilities in controlling circularly polarized waves. However, the geometric PB phase has intrinsically opposite signs for the circularly polarized beams with different helicities. As a result, if a circularly polarized light is focused, then the light with opposite helicity will diverge. The helicity-locked limitation of PB phase metasurfaces can be released by combining the orientation-dependent PB phase and the dimension-dependent propagation phase [50–54]. Here, we propose a bilayer dielectric metasurface that simultaneously employs propagation and geometric phases to realize helicity-dependent continuous varifocal metalens in the near-infrared range. Focal length tuning is achieved by modifying the polarization states of incident waves and crystallization fraction of constituent phase-change Sb_2S_3 meta-atoms. The propagation phase metasurface consists of Sb_2S_3 nanopillars with a square cross-section, where the phase response can be dynamically manipulated by varying the crystallization fraction of Sb_2S_3. Si nanopillars with rectangular cross-sections function as half-wave plates (HWPs) and supply propagation and helicity-dependent geometric phases. They are designed to break the mirrored and locked functionalities for the circular polarization beams with different helicities. The proposed helicity-dependent metalens can independently produce a longitudinal focal spot under the left-hand circularly polarized (LCP) or right-hand circularly polarized (RCP) incident wave. This varifocal metalens exhibits excellent focusing capability with Sb_2S_3 switched between crystalline and amorphous states with the zoom range from 32.5 μm to 37.2 μm (RCP) and from 50.5 μm to 60.9 μm (LCP). As the loss of the Sb_2S_3 is almost zero in both states, the simulated focusing efficiencies are above 75% and 87% for the circularly and linearly polarized waves, respectively, regardless of the Sb_2S_3 state. The proposed metalens can potentially find applications in compact optical communication systems, imaging, and biomedical devices.

2.   Theoretical analysis and design of the metalens

To achieve continuous varifocal metalens, we propose a bilayer meta-atom unit cell [Fig. 1(a)], which comprises of a Si nanopillar in the bottom [Fig. 1(b)] and Sb_2S_3 nanopillar at the top [Fig. 1(c)]. At the selected wavelength of 1550 nm, the refractive index of Si is 3.48 [55], and the refractive indexes of Sb_2S_3 in amorphous and crystalline states are 2.712 and 3.308 [46]. In

particular, the loss of silicon and both states of Sb_2S_3 are negligible at 1550 nm. The Si layer of the metasurface can be defined using electron beam lithography (EBL) and deep reactive ion etching (RIE) followed by encapsulation in a silica layer with the thickness of $h_3 = 2$ μm. Sb_2S_3 layer of thickness $h_2 = 1$ μm can be sputtered onto the chip by thermal co-evaporation or magnetron sputtering. Finally, The phase-change Sb_2S_3 layer can be patterned via EBL followed by RIE process [44]. The schematics of the varifocal metalens with different crystallization factions of Sb_2S_3 are illustrated in Figs. 1(d)–1(i). The metalens will have two different focal lengths, depending on whether the illumination light is RCP or LCP [see Figs. 1(d, e)]. This helicity-dependent focal length can be continuously adjusted by changing Sb_2S_3 from crystalline to amorphous [see Figs. 1(g, h)]. Once the incident wave is switched to a linearly polarized (LP) wave (e.g., x-LP), both helicity-dependent focal spots will appear simultaneously, thereby enabling the multiplexing of helicity-dependent dual foci [Fig. 1(f)]. Similarly, the focal lengths of the dual foci can be changed by transitioning from crystalline Sb_2S_3 (c-Sb_2S_3) to amorphous Sb_2S_3 (a-Sb_2S_3) [Fig. 1(i)].
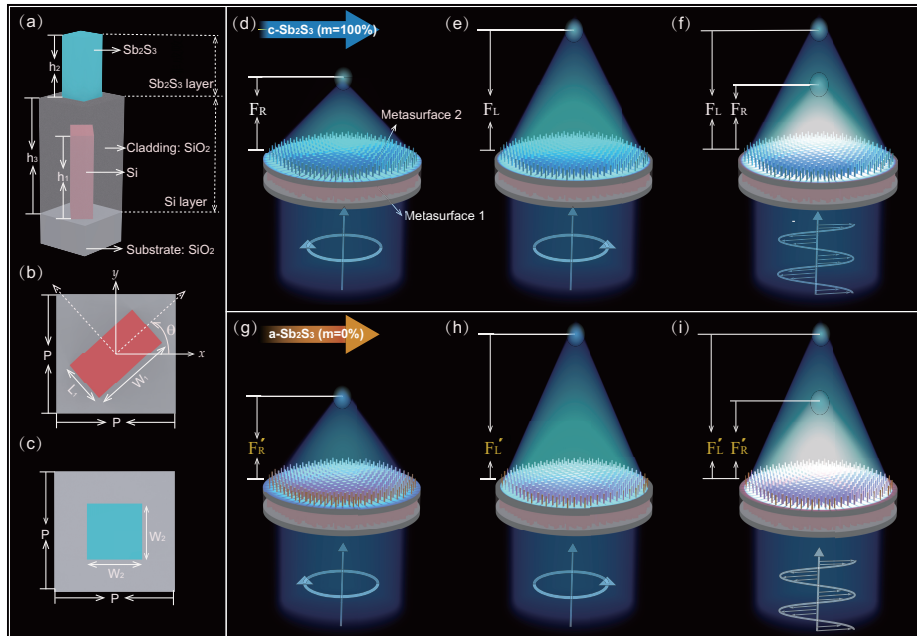
Fig. 1. (a) The schematic of the proposed meta-atom unit cell. (b) The Si layer unit cell. (c) The Sb_2S_3 layer unit cell. The illustration of helicity-controlled continuous varifocal metalens under (d) RCP, (e) LCP, and (f) x-LP waves excitations with Sb_2S_3 in the crystalline state. The illustration of helicity-controlled continuous varifocal metalens under (g) RCP, (h) LCP, and (i) x-LP waves excitations with Sb_2S_3 in the amorphous state.

We design the Si nanopillars that implement both the geometric and propagation phases to independently manipulate two orthogonal circular polarization. Generally, when circularly polarized waves illuminate on the Si nanopillar with rectangular cross-section whose orientation angle is θ relative to the x-axis, the Jones matrix in the circularly polarized base can be expressed by [56]:

$$J(\theta)_{circular} = \begin{bmatrix} \frac{1}{2}(t_{xx} + t_{yy}) & \frac{1}{2}(t_{xx} - t_{yy})e^{j2\theta} \\ \frac{1}{2}(t_{xx} - t_{yy})e^{-j2\theta} & \frac{1}{2}(t_{xx} + t_{yy}) \end{bmatrix} \qquad (1)$$

where t_{xx} and t_{yy} denote the complex transmission coefficients of the Si nanopillars under x- and y-LP incidences. When $t_{xx} = -t_{yy}$, the Si metasurface acts as an HWP. We assume the transmission coefficients t_{xx} can be expressed as $t_{xx} = A_{xx}e^{j\delta_{xx}}$, where δ_{xx} and A_{xx} are the corresponding phase shift and amplitude, respectively. Therefore, the Jones matrix can be simplified as [50]:

$$J(\theta)_{circular} = \begin{bmatrix} 0 & A_{xx}e^{j(\delta_{xx}+2\theta)} \\ A_{xx}e^{j(\delta_{xx}-2\theta)} & 0 \end{bmatrix} \tag{2}$$

By independently controlling the propagation phases with size-varying nanopillars, and the geometric phases with different orientation angles θ, the helicity-dependent phase of $\delta_{xx} \pm 2\theta$ can be imposed on the transmitted LCP and RCP waves, respectively.

In the Sb_2S_3 layer of the metalens, only the propagation phase is controlled by changing the dimensions of Sb_2S_3 nanopillars to adjust the optical response of transmitted waves dynamically. The Sb_2S_3 nanopillars that function as dielectric waveguides can add a phase shift of $\Phi = 2\pi n_{eff}h_2/\lambda_0$ to the transmitted waves, where n_{eff} is the effective index of the fundamental mode and λ_0 is the wavelength in free space. The varifocal function can be realized by changing the effective index of the Sb_2S_3 nanopillars concerning the crystallization fractions. Here, it should be mentioned that the phase shifts of the transmitted waves after passing through the bilayer structures is a linear superposition of the phase shifts of the two layers [57], thereby providing more degrees of freedom for our design.

To realize a high-efficiency varifocal metalens, the commercial 3D finite difference time domain (FDTD) solver is used to optimize the geometries of the Si and Sb_2S_3 nanopillars at the operating wavelength of $\lambda_0 = 1550$ nm. The height h_1 of the Si nanopillars is fixed as 1.5 μm to achieve the desired 2π propagation phase coverage for implementing an HWP. The unit cell pitch P is 600 nm, which ensures that these nanopillars can be regarded as a zeroth-order grating with relatively high transmission in the near-infrared band [58]. Figure 2(a) indicates the simulated circular polarization conversion ratio (PCR) of Si nanopillars as a function of its sizes of W_1 and L_1, which is defined as PCR = $\frac{T_{cross}}{T_{cross}+T_{co}}$, where T_{cross} and T_{co} are the transmission amplitudes of converted and unconverted circularly polarized waves, respectively. From Fig. 2(a), we can select a set of fifteen nanopillars that can work as the HWPs while exhibiting high transmission at the working wavelength for the LP incidences [Fig. 2(b)]. In particular, the phase difference $(|\delta_{xx} - \delta_{yy}|)$ of fifteen nanopillars are all equals to π, satisfying the requirement of HWPs. These HWPs provide fifteen phase levels covering the entire 0-2π range for both δ_{xx} and δ_{yy}.

To gain a better insight into the mechanism of the geometric phase, Fig. 2(c) shows the simulated transmission amplitudes and phase shifts of converted LCP waves versus the rotation angle θ of the 5th and 13th Si nanopillars under RCP excitation. We can see that the phase shifts equal 2θ, and the incident wave is nearly transformed into the corresponding orthogonal component. Regarding the Sb_2S_3 nanopillars, its height h_2 is fixed at 1 μm to ensure high transmission and the desired 2π phase coverage. Figure 2(d) shows the simulated transmission amplitudes and phase delays of the c-Sb_2S_3 nanopillars with the width W_2 varied from 150 to 400 nm for the circularly polarized incidences.

To focus the transmitted waves into the focal point, the spatial variation of the phase distributions should meet the following formula:

$$\varphi_i(x, y, F_i) = \frac{2\pi}{\lambda_0}\left(\sqrt{F_i^2 + x^2 + y^2} - F_i\right) \tag{3}$$

where F_i is the focal length, λ_0 is the working wavelength, and (x, y) represents the in-plane coordinate of each nanopillar. Here, the phase distribution $\varphi_i(x, y, F_i)$ usually refers to geometric phases or propagation phases or even their combination, namely helicity-dependent phases. To produce two well-separated focal points, the Si layer is required to provide two different spatial
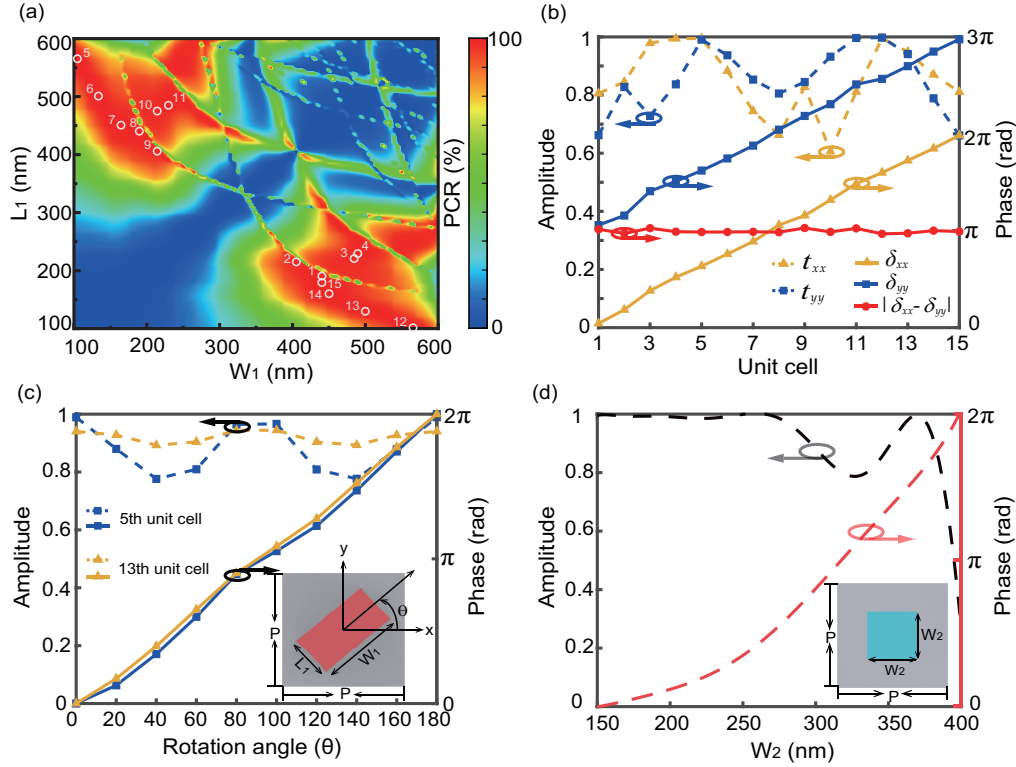
Fig. 2. (a) The simulated polarization conversion ratio (PCR) of the Si nanopillars with different sizes under RCP excitation. The chosen Si HWPs are marked with white circles. (b) The simulated transmission amplitudes (A_{xx} and A_{yy}), phase delays (δ_{xx} and δ_{yy}) and phase difference ($|\delta_{xx} - \delta_{yy}|$) of the fifteen Si nanopillars under LP incidences. (c) The simulated transmission amplitudes and phase shifts of converted LCP waves versus the rotation angle θ of the 5th and 13th Si nanopillars under RCP excitation. (d) The simulated transmission amplitudes and phase delays of the c-Sb_2S_3 nanopillars for the circularly polarized incidences.

phase distributions $\varphi_1(x, y, F_1)$ and $\varphi_2(x, y, F_2)$, respectively, corresponding to RCP and LCP waves. Specifically, this Si layer that can be described by a position-dependent Jones matrix $J(x, y)$ simultaneously implements $J(x, y)|\text{RCP}\rangle = e^{i\varphi_1(x,y,F_1)}|\text{LCP}\rangle$ and $J(x, y)|\text{LCP}\rangle = e^{i\varphi_2(x,y,F_2)}|\text{RCP}\rangle$. Therefore, the required Jones matrix should satisfy the following form [59]:

$$J(x, y) = \begin{bmatrix} \dfrac{e^{i\varphi_1(x,y,F_1)} + e^{i\varphi_2(x,y,F_2)}}{2} & \dfrac{ie^{i\varphi_2(x,y,F_2)} - ie^{i\varphi_1(x,y,F_1)}}{2} \\ \dfrac{ie^{i\varphi_2(x,y,F_2)} - ie^{i\varphi_1(x,y,F_1)}}{2} & \dfrac{-e^{i\varphi_1(x,y,F_1)} - e^{i\varphi_2(x,y,F_2)}}{2} \end{bmatrix} \quad (4)$$

Owing to symmetric and unitary conditions, $J(x, y)$ can be expressed as $J(x, y) = R\Lambda R^{-1}$, where Λ represents a diagonal matrix and R is a real unitary matrix. For Si nanopillars, the diagonal matrix Λ denotes impose phase shifts δ_{xx} and δ_{yy} to LP waves along its long and short axes, while the matrix R corresponds to the orientation angle θ of its long axis relative to the x-axis. Considering the given helicity-dependent phase distributions $\varphi_1(x, y, F_1)$ and $\varphi_2(x, y, F_2)$, the desired phase shifts and orientation angles of Si nanopillars can be written as [59] (Fig. 3):

$$\delta_{xx}(x, y) = \frac{1}{2}[\varphi_1(x, y, F_1) + \varphi_2(x, y, F_2)] \quad (5)$$

$$\delta_{yy}(x, y) = \frac{1}{2}[\varphi_1(x, y, F_1) + \varphi_2(x, y, F_2)] - \pi \tag{6}$$

$$\theta(x, y) = \frac{1}{4}[\varphi_1(x, y, F_1) - \varphi_2(x, y, F_2)] \tag{7}$$
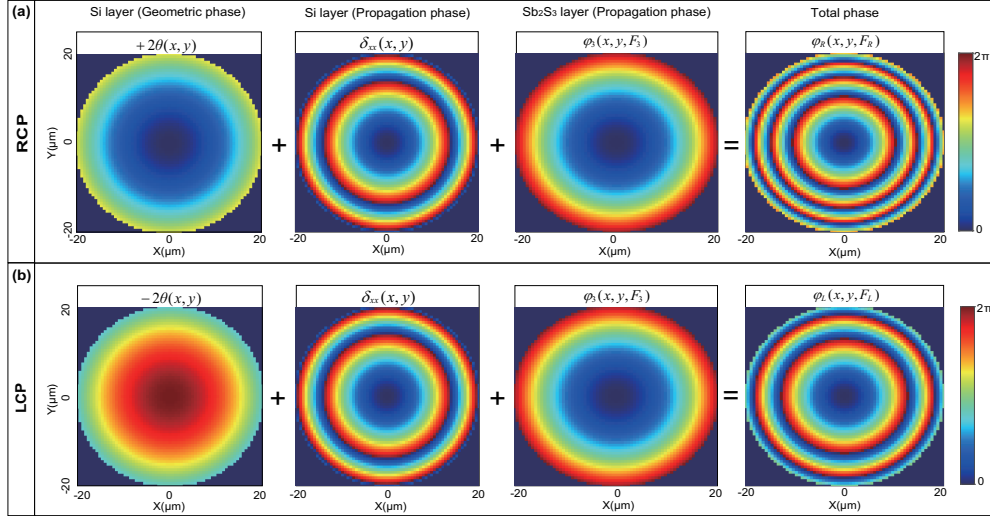
Fig. 3. The phase distributions at each layer under RCP (a) and LCP (b) excitations

According to Eqs. (5–7), the selected fifteen Si nanopillars that function as highly efficient HWPs and provide a propagation phase spanning the entire range from 0 to 2π can be appropriately arranged. For the Sb_2S_3 layer, its phase profiles satisfy $\varphi_3(x, y, F_3)$, which is insensitive to the polarization of incident light. Consequently, the total phase distributions for incident RCP and LCP waves after passing through the metalens can be expressed as [57]:

$$\begin{cases} \varphi_{RCP}(x, y, F_R) = \varphi_1(x, y, F_1) + \varphi_3(x, y, F_3) = \delta_{xx}(x, y) + 2\theta(x, y) + \varphi_3(x, y, F_3) \\ \varphi_{LCP}(x, y, F_L) = \varphi_2(x, y, F_2) + \varphi_3(x, y, F_3) = \delta_{xx}(x, y) - 2\theta(x, y) + \varphi_3(x, y, F_3) \end{cases} \tag{8}$$

The total phase distributions of the two-layer metasurfaces $\varphi_{RCP}(x, y, F_R)$ and $\varphi_{LCP}(x, y, F_L)$ are shown in Fig. 3, from which we can find that such bilayer metasurfaces can also satisfy the focus formula. When a collimated RCP wave illuminates on the metalens, the focus formula with F_R can be write as:

$$\frac{2\pi}{\lambda_0}\left(\sqrt{F_R^2 + x^2 + y^2} - F_R\right) = \varphi_{RCP}(x, y, F_R) \tag{9}$$

The focal length F_R can be obtained by fitting the phase distribution $\varphi_{RCP}(x, y, F_R)$ with the Eq. (9).

In contrast, when a collimated LCP wave illuminates on the metalens, the focus formula with F_L can be expressed as:

$$\frac{2\pi}{\lambda_0}\left(\sqrt{F_L^2 + x^2 + y^2} - F_L\right) = \varphi_{LCP}(x, y, F_L). \tag{10}$$

The focal length F_L can be obtained by fitting the phase distribution $\varphi_{LCP}(x, y, F_L)$ with the Eq. (10).

Hence, the theoretical focal lengths of the metalens are approximately 31.8 μm and 50.2 μm for RCP and LCP waves.

3. Results and discussion

3.1. *Switchable helicity-dependent metalens*

Here, we use the FDTD technique to accurately calculate the transmission properties of the metalens, and the near-to-far-field transformation approach is used to obtain the electric field and magnetic field in the far-field domain to save the calculation time. The simulated performance of the switchable helicity-dependent metalens that can independently generate different focal spots is illustrated in Fig. 4. Figures 4(a) and 4(b) show the intensity profiles of the transmitted waves in the *x-z* plane under the RCP and LCP excitations, respectively. We find the simulated focal lengths of the metalens to be 32.5 μm and 50.5 μm, which are very close to theoretical values. The slight deviation in focal spot positions between the theoretical design and numerical simulation is mainly ascribed to the discrete phase shift between adjacent nanopillars. There is a large discrepancy in the maximum intensity of the two foci due to the difference in the numerical aperture (*NA*), which is calculated by the equation of $NA = \sin[\tan^{-1}(D/2F_i)]$. The calculated *NAs* of the metalens are 0.5 and 0.37 for the RCP and LCP waves. LP waves can be considered as a linear combination of two circularly polarized waves with opposite helicity. Therefore, when an *x*-LP wave impinges on the metalens at normal incidence, the coaxial multiplexing of the helicity-dependent dual foci is realized, as shown in Fig. 4(c). When Sb_2S_3 transitions from c-Sb_2S_3 to a-Sb_2S_3, the transmitted LCP or RCP waves are focused into different longitudinal positions of 37.2 μm and 60.9 μm [In Fig. 4(d) and 4(e)], respectively, and the corresponding *NAs* of the metalens are changed to 0.47 and 0.31. Similarly, two new focal spots are simultaneously generated when Sb_2S_3 is in the amorphous state under *x*-LP excitation, as indicated in Fig. 4(f). After verifying the focusing capability, we calculate the focusing efficiency for the metalens as high as 75% and for the RCP and 77% for LCP incidences, respectively, and the total focusing efficiency of the dual foci metalens upon *x*-LP excitation is found to be 88%. The focusing
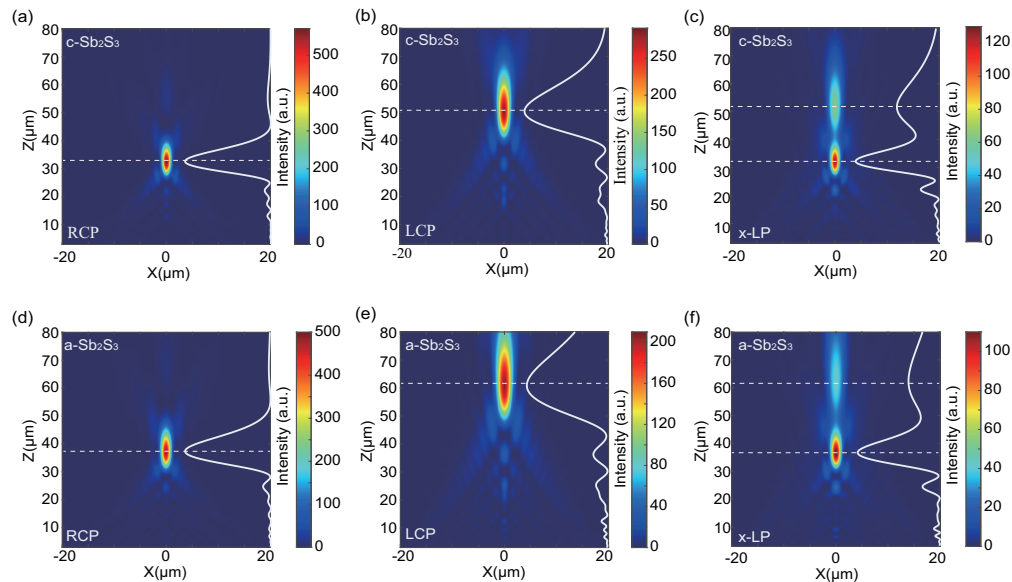
Fig. 4. (a-c) The simulated intensity profiles in the *x-z* plane under the illumination of RCP (a), LCP (b), and *x*-LP (c) waves when Sb_2S_3 is in the crystalline state. (d-f) The simulated intensity profiles in the *x-z* plane under the illumination of RCP (d), LCP (e), and *x*-LP (f) waves when Sb_2S_3 is in the amorphous state. The white curves represent the cross-section of simulated intensity along the *z*-axis.

efficiencies are defined as the energy ratio of a circular area on the focal plane to the incident beam that passes through the metalens. The circular radius on the focal plane is two times the full width half maximum (FWHM) spot size [20].

### 3.2. Helicity-dependent continuous varifocal metalens

The reversible switching between the c-Sb$_2$S$_3$ and a-Sb$_2$S$_3$ can be accomplished by applying laser pulses [45,46] or voltage pulses [45,49] with the designated power for a predefined time duration. Additionally, the intermediate state of Sb$_2$S$_3$ can be perceived as the arbitrary combination of crystalline and amorphous molecules, thereby providing the opportunity for realizing the continuous varifocal metalens. To simulate the response of Sb$_2$S$_3$ meta-atoms with different crystallization fractions, the Lorentz-Lorenz relation is employed to approximate the permittivity of the Sb$_2$S$_3$ [60]:

$$\frac{\varepsilon_{\text{eff}}(\lambda) - 1}{\varepsilon_{\text{eff}}(\lambda) + 2} = m \times \frac{\varepsilon_{\text{c-Sb}_2\text{S}_3}(\lambda) - 1}{\varepsilon_{\text{c-Sb}_2\text{S}_3}(\lambda) + 2} + (1 - m) \times \frac{\varepsilon_{\text{a-Sb}_2\text{S}_3}(\lambda) - 1}{\varepsilon_{\text{a-Sb}_2\text{S}_3}(\lambda) + 2} \tag{11}$$

where $\varepsilon_{\text{c-Sb}_2\text{S}_3}(\lambda)$ and $\varepsilon_{\text{a-Sb}_2\text{S}_3}(\lambda)$ represent the permittivity of c-Sb$_2$S$_3$ and a-Sb$_2$S$_3$, respectively, and m is the crystallization fraction of Sb$_2$S$_3$ ranging from 100% to 0%. To demonstrate the continuous varifocal properties of the proposed metalens, we investigate the optical response of the Sb$_2$S$_3$ nanopillars with varied crystallization fraction m. Figures 5(a) and 5(b) show the phase shifts and transmission amplitudes as a function of the nanopillar widths with different crystallization fractions. The phase shifts can be adjusted by changing the state of the Sb$_2$S$_3$ nanopillars while the transmission amplitudes are maintained at high levels, implying high focusing efficiency. Figure 5(c) indicates the calculated phase distributions in the x-direction of the Sb$_2$S$_3$ layer within the metalens when the crystallization fraction m is gradually decreased from 100% to 0%. Impressively, these phase distributions resemble the ideal parabolic profiles, manifesting that the metalens can always maintain an excellent focusing performance when Sb$_2$S$_3$ is reconfigured between the crystalline and amorphous states. Figures 6(a) and 6(b) denote the intensity distributions in the x-z plane of transmitted LCP and RCP waves after passing through the metalens, respectively. One can observe that the maximum intensity in the focal spot decreases with the reduced crystallization fraction m, which is attributed to the increase of the focal length and consequently reduced *NA*. In Fig. 6(c), the intensity profiles of transmitted LCP and RCP waves are plotted under the excitation of an x-LP wave. It should be noted that the zoom range of the second focal point is larger than that of the first focal point since the zoom range of each focal spot is proportional to the designed focal length within a certain range.
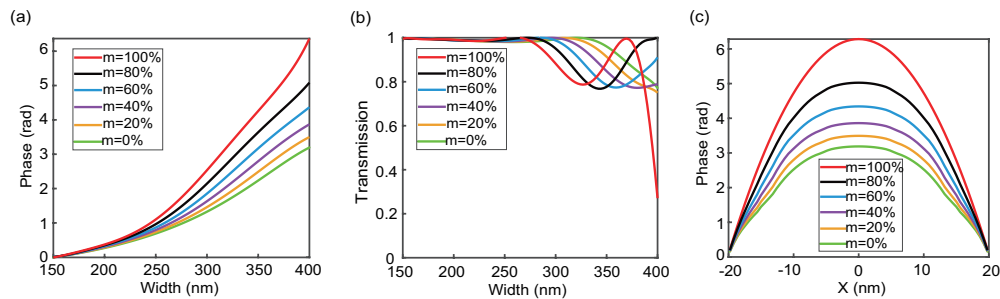
Fig. 5. The phase shifts (a) and transmission amplitudes (b) of the Sb$_2$S$_3$ nanopillars with different crystallization fractions as a function of the nanopillars width. (c) The calculated phase distributions in the x-direction of the Sb$_2$S$_3$ layer within the metalens with different crystallization fractions.
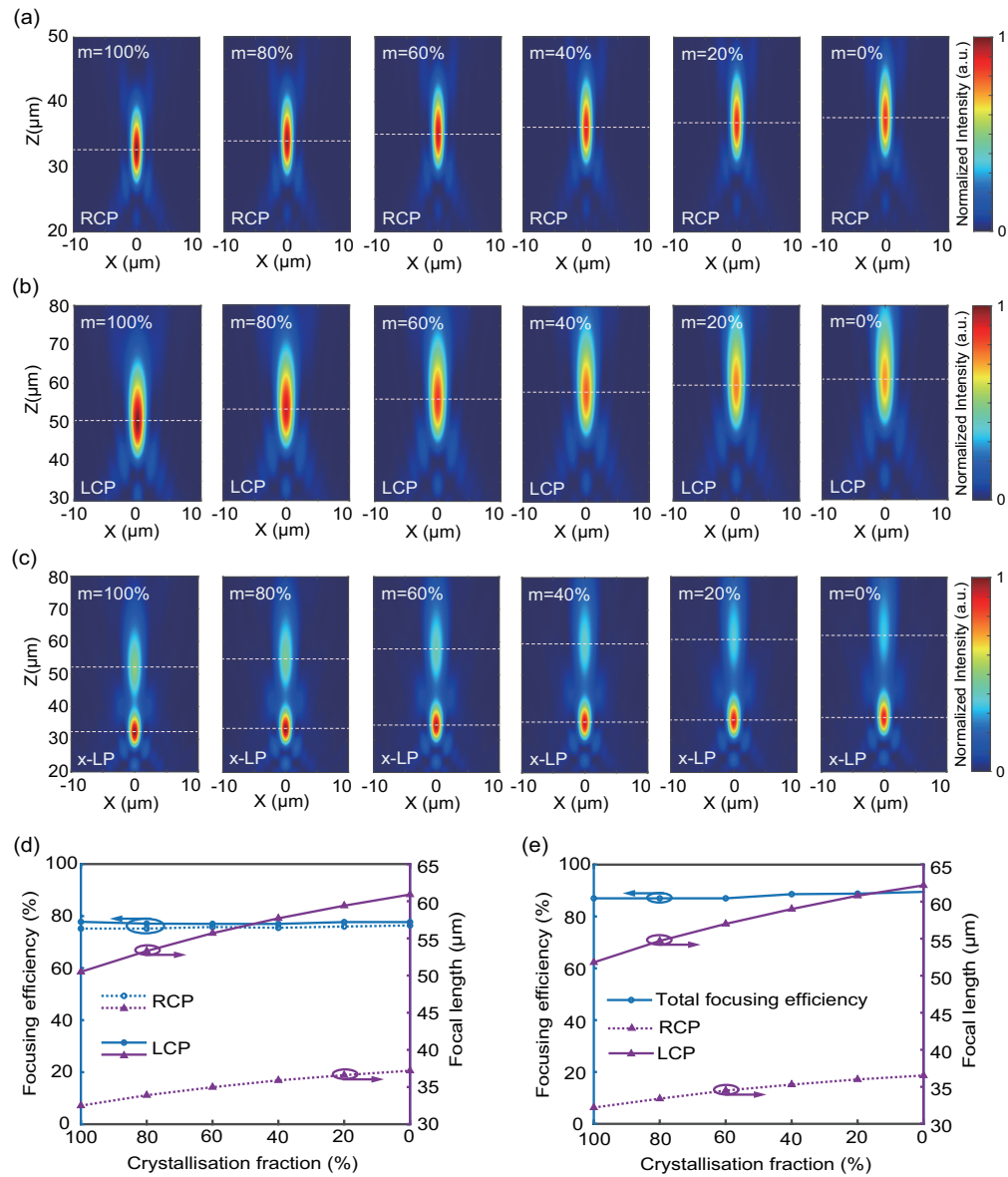
Fig. 6. The intensity profiles in the *x-z* plane under the illumination of RCP (a), LCP (b), and *x*-LP (c) waves when Sb_2S_3 has a different crystallization fraction. (d) The corresponding focal length and focusing efficiency of the two focal points versus crystallization fractions upon the illumination of RCP and LCP waves. (e) The corresponding focal length and total focusing efficiency of the dual foci versus crystallization fraction upon the illumination of an *x*-LP wave.

Figure 6(d) summarizes the focusing efficiency and focal length of the two foci as a function of the crystallization fraction. When the RCP wave is incident on the metalens, a zoom range of 4.7 μm is achieved with an average focusing efficiency of 75%. When the LCP wave impinges, the zoom range is increased to 10.4 μm, and the average focusing efficiency reaches 77%. Figure 6(e)

shows that the similar focusing efficiency and focal length of the two foci under an *x*-LP incident wave, the total focusing efficiency remains to be 88%.

4. Conclusion

In conclusion, we have demonstrated a kind of helicity-dependent metalens based on the spin decoupled metasurface by combining propagation phase and geometric phase, which also has continuous varifocal properties due to the phase change material. The spin-decoupled metasurface is composed of Si nanopillars that function as HWPs and simultaneously implement propagation and geometric phases. While combined with low-loss phase-change Sb_2S_3 nanopillars, the focal length of the whole metalens structure can be modulated by changing the crystallization fraction of the Sb_2S_3 nanopillars. We do note that, however, changing the whole micron-thick phase change materials will be an experimentally challenging task. Upon excitation with the RCP or LCP wave, the metalens can generate helicity-dependent longitudinal focal spots with focal lengths continuously adjusted by modifying the crystallization fraction of Sb_2S_3. The zoom range is achieved from 32.5 μm to 37.2 μm and for RCP and from 50.5 μm to 60.9 μm for LCP, respectively. The simulated focusing efficiencies are above 75% and 87% for circularly and linearly polarized waves, due to near-zero loss of the Sb_2S_3. Due to the high efficiency, tunable focal length, and arbitrary intensity ratio between two foci, the metalens can find many applications in various fields, such as multi-imaging systems, biomedical science, and optical tomography techniques.

Disclosures. The authors declare no conflicts of interest.

Data availability. Data underlying the results presented in this paper are not publicly available at this time but may be obtained from the authors upon reasonable request.

References

1. F. Aieta, M. A. Kats, P. Genevet, and F. Capasso, "Multiwavelength achromatic metasurfaces by dispersive phase compensation," Science **347**(6228), 1342–1345 (2015).
2. R. C. Devlin, A. Ambrosio, N. A. Rubin, J. P. B. Mueller, and F. Capasso, "Arbitrary spin-to–orbital angular momentum conversion of light," Science **358**(6365), 896–901 (2017).
3. X. Zang, H. Gong, Z. Li, J. Xie, Q. Cheng, L. Chen, A. P. Shkurinov, Y. Zhu, and S. Zhuang, "Metasurface for multi-channel terahertz beam splitters and polarization rotators," Appl. Phys. Lett. **112**(17), 171111 (2018).
4. F. Ding, A. Pors, and S. I. Bozhevolnyi, "Gradient metasurfaces: a review of fundamentals and applications," Rep. Prog. Phys. **81**(2), 026401 (2018).
5. S. Sun, Q. He, S. Xiao, Q. Xu, X. Li, and L. Zhou, "Gradient-index meta-surfaces as a bridge linking propagating waves and surface waves," Nat. Mater. **11**(5), 426–431 (2012).
6. N. Yu, F. Aieta, P. Genevet, M. A. Kats, Z. Gaburro, and F. Capasso, "A Broadband, Background-Free Quarter-Wave Plate Based on Plasmonic Metasurfaces," Nano Lett. **12**(12), 6328–6333 (2012).
7. J. Xu, R. Li, S. Wang, and T. Han, "Ultra-broadband linear polarization converter based on anisotropic metasurface," Opt. Express **26**(20), 26235–26241 (2018).
8. S. Teng, Q. Zhang, H. Wang, L. Liu, and H. Lv, "Conversion between polarization states based on a metasurface," Photonics Res. **7**(3), 246–250 (2019).
9. F. Ding, R. Deshpande, C. Meng, and S. I. Bozhevolnyi, "Metasurface-enabled broadband beam splitters integrated with quarter-wave plate functionality," Nanoscale **12**(26), 14106–14111 (2020).
10. F. Ding, S. Tang, and S. I. Bozhevolnyi, "Recent Advances in Polarization-Encoded Optical Metasurfaces," Adv. Photonics Res. **2**(6), 2000173 (2021).
11. K. Ou, G. Li, T. Li, H. Yang, F. Yu, J. Chen, Z. Zhao, G. Cao, X. Chen, and W. Lu, "High efficiency focusing vortex generation and detection with polarization-insensitive dielectric metasurfaces," Nanoscale **10**(40), 19154–19161 (2018).
12. S. Li, X. Li, L. Zhang, G. Wang, L. Zhang, M. Liu, C. Zeng, L. Wang, Q. Sun, W. Zhao, and W. Zhang, "Efficient Optical Angular Momentum Manipulation for Compact Multiplexing and Demultiplexing Using a Dielectric Metasurface," Adv. Opt. Mater. **8**(8), 1901666 (2020).
13. F. Ding, Y. Chen, and S. I. Bozhevolnyi, "Focused vortex-beam generation using gap-surface plasmon metasurfaces," Nanophotonics **9**(2), 371–378 (2020).

14. W. Luo, S. Sun, H.-X. Xu, Q. He, and L. Zhou, "Transmissive Ultrathin Pancharatnam-Berry Metasurfaces with nearly 100% Efficiency," Phys. Rev. Appl. **7**(4), 044033 (2017).

15. G. Zheng, H. Mühlenbernd, M. Kenney, G. Li, T. Zentgraf, and S. Zhang, "Metasurface holograms reaching 80% efficiency," Nat. Nanotechnol. **10**(4), 308–312 (2015).

16. H. Ren, X. Fang, J. Jang, J. Bürger, J. Rho, and S. A. Maier, "Complex-amplitude metasurface-based orbital angular momentum holography in momentum space," Nat. Nanotechnol. **15**(11), 948–955 (2020).

17. M. Khorasaninejad, W. T. Chen, R. C. Devlin, J. Oh, A. Y. Zhu, and F. Capasso, "Metalenses at visible wavelengths: Diffraction-limited focusing and subwavelength resolution imaging," Science **352**(6290), 1190–1194 (2016).

18. M. Khorasaninejad, A. Y. Zhu, C. Roques-Carmes, W. T. Chen, J. Oh, I. Mishra, R. C. Devlin, and F. Capasso, "Polarization-Insensitive Metalenses at Visible Wavelengths," Nano Lett. **16**(11), 7229–7234 (2016).

19. H. Liang, Q. Lin, X. Xie, Q. Sun, Y. Wang, L. Zhou, L. Liu, X. Yu, J. Zhou, T. F. Krauss, and J. Li, "Ultrahigh Numerical Aperture Metalens at Visible Wavelengths," Nano Lett. **18**(7), 4460–4466 (2018).

20. L. Chen, Y. Hao, L. Zhao, R. Wu, Y. Liu, Z. Wei, N. Xu, Z. Li, and H. Liu, "Multifunctional metalens generation using bilayer all-dielectric metasurfaces," Opt. Express **29**(6), 9332–9345 (2021).

21. F. Ding, B. Chang, Q. Wei, L. Huang, X. Guan, and S. I. Bozhevolnyi, "Versatile Polarization Generation and Manipulation Using Dielectric Metasurfaces," Laser Photonics Rev. **14**(11), 2000116 (2020).

22. S. Wang, P. C. Wu, V.-C. Su, Y.-C. Lai, M.-K. Chen, H. Y. Kuo, B. H. Chen, Y. H. Chen, T.-T. Huang, J.-H. Wang, R.-M. Lin, C.-H. Kuan, T. Li, Z. Wang, S. Zhu, and D. P. Tsai, "A broadband achromatic metalens in the visible," Nat. Nanotechnol. **13**(3), 227–232 (2018).

23. A. She, S. Zhang, S. Shian, D. R. Clarke, and F. Capasso, "Adaptive metalenses with simultaneous electrical control of focal length, astigmatism, and shift," Sci. Adv. **4**, eaap9957 (2018).

24. M. B. Kumar, D. Kang, J. Jung, H. Park, J. Hahn, M. Choi, J.-H. Bae, H. Kim, and J. Park, "Compact vari-focal augmented reality display based on ultrathin, polarization-insensitive, and adaptive liquid crystal lens," Opt. Lasers Eng. **128**, 106006 (2020).

25. S. Wei, G. Cao, H. Lin, X. Yuan, M. Somekh, and B. Jia, "A Varifocal Graphene Metalens for Broadband Zoom Imaging Covering the Entire Visible Region," ACS Nano **15**(3), 4769–4776 (2021).

26. E. Arbabi, A. Arbabi, S. M. Kamali, Y. Horie, M. Faraji-Dana, and A. Faraon, "MEMS-tunable dielectric metasurface lens," Nat. Commun. **9**(1), 812 (2018).

27. C. Meng, P. C. V. Thrane, F. Ding, J. Gjessing, M. Thomaschewski, C. Wu, C. Dirdal, and S. I. Bozhevolnyi, "Dynamic piezoelectric MEMS-based optical metasurfaces," Sci. Adv. **7**(26), eabg5639 (2021).

28. Z. Han, S. Colburn, A. Majumdar, and K. F. Böhringer, "MEMS-actuated metasurface Alvarez lens," Microsyst. Nanoeng. **6**(1), 79 (2020).

29. H.-S. Ee and R. Agarwal, "Tunable Metasurface and Flat Optical Zoom Lens on a Stretchable Substrate," Nano Lett. **16**(4), 2818–2823 (2016).

30. S. M. Kamali, E. Arbabi, A. Arbabi, Y. Horie, and A. Faraon, "Highly tunable elastic dielectric metasurface lenses," Laser Photonics Rev. **10**(6), 1002–1008 (2016).

31. C.-H. Liu, J. Zheng, S. Colburn, T. K. Fryett, Y. Chen, X. Xu, and A. Majumdar, "Ultrathin van der Waals Metalenses," Nano Lett. **18**(11), 6961–6966 (2018).

32. Y. Cui, G. Zheng, M. Chen, Y. Zhang, Y. Yang, J. Tao, T. He, and Z. Li, "Reconfigurable continuous-zoom metalens in visible band," Chin. Opt. Lett. **17**(11), 111603 (2019).

33. Y. Guo, M. Pu, X. Ma, X. Li, R. Shi, and X. Luo, "Experimental demonstration of a continuous varifocal metalens with large zoom range and high imaging resolution," Appl. Phys. Lett. **115**(16), 163103 (2019).

34. N. Yilmaz, A. Ozdemir, A. Ozer, and H. Kurt, "Rotationally tunable polarization-insensitive single and multifocal metasurface," J. Opt. **21**(4), 045105 (2019).

35. K. Iwami, C. Ogawa, T. Nagase, and S. Ikezawa, "Demonstration of focal length tuning by rotational varifocal moiré metalens in an ir-A wavelength," Opt. Express **28**(24), 35602–35614 (2020).

36. S. Colburn, A. Zhan, and A. Majumdar, "Varifocal zoom imaging with large area focal length adjustable metalenses," Optica **5**(7), 825–831 (2018).

37. A. Zhan, S. Colburn, C. M. Dodson, and A. Majumdar, "Metasurface Freeform Nanophotonics," Sci. Rep. **7**(1), 1673 (2017).

38. P. Ding, Y. Li, L. Shao, X. Tian, J. Wang, and C. Fan, "Graphene aperture-based metalens for dynamic focusing of terahertz waves," Opt. Express **26**(21), 28038–28050 (2018).

39. Z. Zhang, X. Qi, J. Zhang, C. Guo, and Z. Zhu, "Graphene-enabled electrically tunability of metalens in the terahertz range," Opt. Express **28**(19), 28101–28112 (2020).

40. C.-Y. Fan, T.-J. Chuang, K.-H. Wu, and G.-D. J. Su, "Electrically modulated varifocal metalens combined with twisted nematic liquid crystals," Opt. Express **28**(7), 10609–10617 (2020).

41. M. Bosch, M. R. Shcherbakov, K. Won, H.-S. Lee, Y. Kim, and G. Shvets, "Electrically actuated varifocal lens based on liquid-crystal-embedded dielectric metasurfaces," Nano Lett. **21**(9), 3849–3856 (2021).

42. X. Yin, T. Steinle, L. Huang, T. Taubner, M. Wuttig, T. Zentgraf, and H. Giessen, "Beam switching and bifocal zoom lensing using active plasmonic metasurfaces," Light: Sci. Appl. **6**(7), e17016 (2017).

43. S. Li, C. Zhou, G. Ban, H. Wang, H. Lu, and Y. Wang, "Active all-dielectric bifocal metalens assisted by germanium antimony telluride," J. Phys. D: Appl. Phys. **52**(9), 095106 (2019).

44. M. Y. Shalaginov, S. An, Y. Zhang, F. Yang, P. Su, V. Liberman, J. B. Chou, C. M. Roberts, M. Kang, C. Rios, Q. Du, C. Fowler, A. Agarwal, K. A. Richardson, C. Rivero-Baleine, H. Zhang, J. Hu, and T. Gu, "Reconfigurable all-dielectric metalens with diffraction-limited performance," Nat. Commun. **12**(1), 1225 (2021).

45. W. Dong, H. Liu, J. K. Behera, L. Lu, R. J. H. Ng, K. V. Sreekanth, X. Zhou, J. K. W. Yang, and R. E. Simpson, "Wide Bandgap Phase Change Material Tuned Visible Photonics," Adv. Funct. Mater. **29**(6), 1806181 (2019).

46. M. Delaney, I. Zeimpekis, D. Lawson, D. W. Hewak, and O. L. Muskens, "A New Family of Ultralow Loss Reversible Phase-Change Materials for Photonic Integrated Circuits: Sb2S3 and Sb2Se3," Adv. Funct. Mater. **30**(36), 2002447 (2020).

47. J. Faneca, L. Trimby, I. Zeimpekis, M. Delaney, D. W. Hewak, F. Y. Gardes, C. D. Wright, and A. Baldycheva, "On-chip sub-wavelength Bragg grating design based on novel low loss phase-change materials," Opt. Express **28**(11), 16394–16406 (2020).

48. C. Ruiz de Galarreta, I. Sinev, A. M. Alexeev, P. Trofimov, K. Ladutenko, S. Garcia-Cuevas Carrillo, E. Gemo, A. Baldycheva, J. Bertolotti, and C. David Wright, "Reconfigurable multilevel control of hybrid all-dielectric phase-change metasurfaces," Optica **7**(5), 476–484 (2020).

49. Z. Fang, J. Zheng, A. Saxena, J. Whitehead, Y. Chen, and A. Majumdar, "Non-Volatile Reconfigurable Integrated Photonics Enabled by Broadband Low-Loss Phase Change Material," Adv. Opt. Mater. **9**(9), 2002049 (2021).

50. C. Meng, S. Tang, F. Ding, and S. I. Bozhevolnyi, "Optical Gap-Surface Plasmon Metasurfaces for Spin-Controlled Surface Plasmon Excitation and Anomalous Beam Steering," ACS Photonics **7**(7), 1849–1856 (2020).

51. Q. Fan, M. Liu, C. Zhang, W. Zhu, Y. Wang, P. Lin, F. Yan, L. Chen, H. J. Lezec, Y. Lu, A. Agrawal, and T. Xu, "Independent Amplitude Control of Arbitrary Orthogonal States of Polarization via Dielectric Metasurfaces," Phys. Rev. Lett. **125**(26), 267402 (2020).

52. P. Huo, C. Zhang, W. Zhu, M. Liu, S. Zhang, S. Zhang, L. Chen, H. J. Lezec, A. Agrawal, Y. Lu, and T. Xu, "Photonic Spin-Multiplexing Metasurface for Switchable Spiral Phase Contrast Imaging," Nano Lett. **20**(4), 2791–2798 (2020).

53. S. Li, Z. Wang, S. Dong, S. Yi, F. Guan, Y. Chen, H. Guo, Q. He, L. Zhou, and S. Sun, "Helicity-delinked manipulations on surface waves and propagating waves by metasurfaces," Nanophotonics **9**(10), 3473–3481 (2020).

54. Z. Wang, S. Li, X. Zhang, X. Feng, Q. Wang, J. Han, Q. He, W. Zhang, S. Sun, and L. Zhou, "Excite Spoof Surface Plasmons with Tailored Wavefronts Using High-Efficiency Terahertz Metasurfaces," Adv. Sci. **7**(19), 2000982 (2020).

55. D. T. Pierce and W. E. Spicer, "Electronic Structure of Amorphous Si from Photoemission and Optical Studies," Phys. Rev. B **5**(8), 3017–3029 (1972).

56. H.-H. Hsiao, C. H. Chu, and D. P. Tsai, "Fundamentals and Applications of Metasurfaces," Small Methods **1**(4), 1600064 (2017).

57. Y. Zhou, I. I. Kravchenko, H. Wang, J. R. Nolen, G. Gu, and J. Valentine, "Multilayer Noninteracting Dielectric Metasurfaces for Multiwavelength Metaoptics," Nano Lett. **18**(12), 7529–7537 (2018).

58. A. Arbabi, Y. Horie, M. Bagheri, and A. Faraon, "Dielectric metasurfaces for complete control of phase and polarization with subwavelength spatial resolution and high transmission," Nat. Nanotechnol. **10**(11), 937–943 (2015).

59. M. Liu, P. Huo, W. Zhu, C. Zhang, S. Zhang, M. Song, S. Zhang, Q. Zhou, L. Chen, H. J. Lezec, A. Agrawal, Y. Lu, and T. Xu, "Broadband generation of perfect Poincaré beams via dielectric spin-multiplexed metasurface," Nat. Commun. **12**(1), 2230 (2021).

60. C. D. Wright, Y. Liu, K. I. Kohary, M. M. Aziz, and R. J. Hicken, "Arithmetic and Biologically-Inspired Computing Using Phase-Change Materials," Adv. Mater. **23**(30), 3408–3413 (2011).